

Electronic and optical properties of doped TiO_2 by many-body perturbation theory

Michael O. Atambo,^{1,2} Daniele Varsano,^{1,*} Andrea Ferretti,¹ S. Samaneh Ataei,¹ Marilia J. Caldas,³ Elisa Molinari,^{1,2} and Annabella Selloni⁴

¹*Centro S3, CNR-Istituto Nanoscienze, 41125 Modena, Italy*

²*Department of Physics, Mathematics, and Informatics, University of Modena and Reggio Emilia, 41125 Modena, Italy*

³*Instituto de Física, Universidade de São Paulo,*

Cidade Universitária, 05508-900 São Paulo, Brazil

⁴*Department of Chemistry, Princeton University, Princeton, NJ*

(Dated: February 26, 2022)

Doping is one of the most common strategies for improving the photocatalytic and solar energy conversion properties of TiO_2 , hence an accurate theoretical description of the electronic and optical properties of doped TiO_2 is of both scientific and practical interest. In this work we use many-body perturbation theory techniques to investigate two typical n-type dopants, Niobium and Hydrogen, in TiO_2 rutile. Using the GW approximation to determine band edges and defect energy levels, and the Bethe Salpeter equation for the calculation of the absorption spectra, we find that the defect energy levels form non-dispersive bands lying $\simeq 2.2$ eV above the top of the corresponding valence bands ($\simeq 0.9$ eV below the conduction bands of the *pristine* material). The defect states are also responsible for the appearance of low energy absorption peaks that enhance the solar spectrum absorption of rutile. The spatial distributions of the excitonic wavefunctions associated with these low energy excitations are very different for the two dopants, suggesting a larger mobility of photoexcited electrons in Nb- TiO_2 .

PACS numbers:

I. INTRODUCTION

Titanium dioxide (TiO_2) is widely used in photocatalysis and solar energy conversion, but its efficiency is limited by the large band gap (~ 3.0 and 3.2 eV for rutile and anatase, respectively) that severely reduces the photoabsorption of visible light^{1,2}. To improve the conductivity and photocatalytic properties, doping is often employed, and a large variety of dopants, both metals and non-metals, have been explored.^{3,4} Numerous computational studies of doped TiO_2 have also been reported.^{5,6} In this context, studies including an accurate theoretical description of the band gap and impurity levels combined with a detailed analysis of the influence of doping on the optical absorption can contribute new insights of scientific and practical interest as well.

Two of the most common dopants in TiO_2 are Niobium and atomic Hydrogen. They both act as donors, with Nb substituting a Ti atom, and Hydrogen forming an interstitial defect bound to an Oxygen of the lattice.⁵ Nb is usually described as a shallow donor that greatly improves the electrical conductivity of TiO_2 .⁷ At the same time, however, valence-band photoemission spectra of Nb-doped rutile show a peak at about 0.8-1.0 eV below the Fermi energy, indicating an electron in a localized Ti^{3+} state similar to that observed in Oxygen deficient rutile.⁸ This apparent contradiction between ultraviolet photoelectron spectroscopy (UPS) and electrical measurements can be explained within a small polaron model, where the vertical excitation energy of the polaron, as observed in UPS, can be much larger than the energy of adiabatic excitations involved in electrical mea-

surements.⁵ It is generally agreed that the polaron model applies to most defects and impurities in rutile, including interstitial Hydrogen.⁹⁻¹¹ In particular, recent infrared absorption measurements in reduced and hydrogenated rutile have been interpreted on the basis of hybrid density functional calculations, where the self-trapping energy of a conduction band electron to form a localized Ti^{3+} ion was predicted to be ~ 0.3 eV.¹⁰

The electronic structure of doped TiO_2 has been the subject of many theoretical studies. It is now widely accepted that while standard local and semi-local Density Functional Theory (DFT) do not adequately describe the polaronic character of defect and impurity states in TiO_2 , DFT+U and hybrid functionals are effective in determining the structure and energetics of the polaronic states. However, also these approaches are insufficient for precisely describing the electronic energy levels. For instance, hybrid functionals often overestimate the TiO_2 band gap thus leading to an uncertainty in the position of the impurity levels.¹² Recent many-body perturbation theory (MBPT) studies¹³⁻¹⁶ of the band structure and absorption spectrum of pristine TiO_2 have in fact provided evidence that approaches beyond DFT are required for a quantitative description of photoemission and light absorption experiments in this material.

The aim of this work is to investigate the electronic structure and optical properties of Nb- and H-doped TiO_2 , using a rigorous approach that goes beyond mean-field theory. We adopt MBPT, namely the GW approximation for the quasi-particle energies and the Bethe Salpeter equation for the optical spectra. Following a description of the adopted methodology and computational details in Sec. II, our results for the quasi-particle

electronic structure and optical properties are presented and discussed in Sec. III. Conclusions are presented in Sec. IV. We find that both Nb and H doping introduce optically allowed transitions well below the intrinsic optical gap of rutile, thus improving its ability to absorb the solar energy.

II. METHODS

A. Ground state calculations

Ground state calculations were performed using Kohn-Sham (KS) DFT¹⁷ within the plane wave-pseudopotential scheme, as implemented in the Quantum ESPRESSO package.^{18,19} We used the gradient-corrected GGA-PBE²⁰ exchange-correlation functional and norm-conserving ONCV pseudopotentials,²¹ including the semi-core states for Titanium (3s and 3p). We obtained converged KS eigenstates and eigenvalues using a wavefunction kinetic energy cut-off of 80 Ry.

Doped rutile was modelled using a $2 \times 2 \times 3$ supercell (SC) containing 72 atoms (73 atoms in the case of H doping), including one Nb replacing a Ti atom (one interstitial H impurity), which corresponds to a dopant concentration of $\sim 4\%$ (referred to the number of Ti ions). With this SC, reciprocal space was sampled using a Monkhorst-Pack grid of $2 \times 2 \times 2$. For the sake of comparison, pristine rutile was modelled using both the same SC and the primitive cell with an equivalent \mathbf{k} -point sampling. We verified that the two descriptions provide equivalent results, and therefore in the following only the results obtained using the $2 \times 2 \times 3$ supercell are reported.

Relaxed geometries for both pristine and defective TiO_2 were computed including a Hubbard-U term²² in the Ti 3d orbitals. This scheme has been shown to work well for the description of polaronic effects in TiO_2 , particularly for U values in the range 3-4 eV.²³⁻²⁶ Here we use $U = 3.5$ eV, a value close to that given by linear response theory,²⁵ that has been extensively tested and validated in previous studies²⁷⁻³⁰ With this choice, the computed cell parameters of pristine TiO_2 rutile are $a = 4.64 \text{ \AA}$ and $c = 2.96 \text{ \AA}$, in good agreement with the experimental values, $a = 4.59 \text{ \AA}$ and $c = 2.95 \text{ \AA}$.³¹

B. MBPT calculations

The electronic and optical properties of pristine and doped rutile TiO_2 were investigated using the GW method for the self energy operator Σ and the Bethe-Salpeter equation (BSE) for the absorption spectra.³²⁻³⁶ Specifically, we used the single-shot G_0W_0 approximation by treating the frequency dependence of the dielectric matrix via the Godby-Needs (GN) plasmon-pole model (PPM).³⁷

All the MBPT calculations were carried out using the plane-wave code Yambo.^{38,39} In the G_0W_0 calcu-

lations, converged results were obtained by considering 1200 bands (corresponding to 59.53 eV above the energy of the top of the valence band), and a kinetic energy cut-off of 8 Ry for the screening dielectric matrix. GW corrections were introduced on top of DFT-PBE calculations, without the inclusion of Hubbard U. The Bethe-Salpeter equation was built considering vertical transitions involving 20 occupied and 40 empty bands.

In the single shot G_0W_0 approximation, G_0 is built from single particle KS orbitals, and the quasi-particle energies are obtained as a first order perturbation correction. In practice, quasi-particle (QP) energies are obtained as:

$$E_{n\mathbf{k}}^{QP} = \epsilon_{n\mathbf{k}} + Z_{n\mathbf{k}} [\Sigma_{n\mathbf{k}}(\epsilon_{n\mathbf{k}}) - v_{n\mathbf{k}}^{xc}], \quad (1)$$

where $\epsilon_{n\mathbf{k}}$ are the KS eigenvalues, $\Sigma_{n\mathbf{k}}(\omega)$ and $v_{n\mathbf{k}}^{xc}$ are the expectation values of the self-energy and the exchange correlation potential, respectively, over the $n\mathbf{k}$ KS-eigenvector, and $Z_{n\mathbf{k}}$ the QP renormalization factor defined as:

$$Z_{n\mathbf{k}} = \left[1 - \frac{\partial \Sigma_{n\mathbf{k}}(\omega)}{\partial \omega} \Big|_{\omega=\epsilon_{n\mathbf{k}}} \right]^{-1}. \quad (2)$$

The optical properties were calculated by solving the BSE whose kernel includes local field effects as well as the screened electron-hole interaction (with static screening). We also applied the Tamm-Dancoff approximation, which neglects the coupling terms between resonant and anti-resonant blocks, after having numerically verified its validity.

As an analysis tool, we computed atomically-projected DOS (pDOS) with the inclusion of GW QP corrections obtained by Yambo, according to:

$$\rho(\omega) = \frac{1}{N_{\mathbf{k}}} \sum_{\alpha} \sum_{n\mathbf{k}} |\langle \phi_{\alpha} | \psi_{n\mathbf{k}} \rangle|^2 \delta(\omega - E_{n\mathbf{k}}^{QP}), \quad (3)$$

where $|\phi_{\alpha}\rangle$ are atomic orbitals.

Quasi particle unfolded band structures for the doped systems⁴⁰⁻⁴² were calculated considering the spectral function $A(\boldsymbol{\kappa}, \omega)$, resolved with respect to the $\boldsymbol{\kappa}$ -vectors of the host pristine primitive cell (PC),

$$A(\boldsymbol{\kappa}, \omega) = \sum_{mn} |\langle \psi_{m\boldsymbol{\kappa}}^{PC} | \psi_{n\mathbf{k}}^{SC} \rangle|^2 \delta(\omega - E_{n\mathbf{k}}^{QP}), \quad (4)$$

where $\mathbf{k} = \mathbf{k}(\boldsymbol{\kappa})$ according to the folding induced by the supercell, and $|\psi_{m\boldsymbol{\kappa}}^{PC}\rangle$'s form a complete set with $\boldsymbol{\kappa}$ symmetry. Such band structures were obtained using the implementation of the unfolding procedure described in Refs. [41,42].

III. RESULTS

A. Structural properties

The calculated structural parameters for pristine and doped rutile are summarized in Tab. I. In pristine rutile two slightly different Ti-O bond lengths are present,

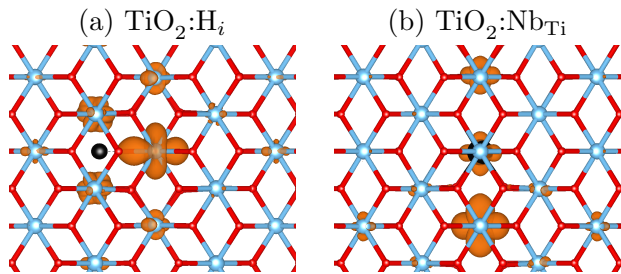


FIG. 1: Relaxed structures of H (left) and Nb-doped (right) rutile TiO₂, viewed along the [010] direction. The spin density isosurface (in orange) is localized on the Ti (and Nb) atoms near the defect center. Dopants (H and Nb) are in black.

TABLE I: Bond lengths (in Å) for pristine and doped rutile TiO₂. For the doped systems, maximum and minimum values of type I and type II Ti-O bond lengths are given. Distances between the dopant and Ti (D-Ti) and O (D-O) are also reported.

bond	TiO ₂	TiO ₂ :H _i	TiO ₂ :Nb _{Ti}
Ti-O	type I 1.96	1.91 - 2.07	1.90 - 2.07
	type II 1.99	1.94 - 2.03	1.94 - 2.01
D-Ti		2.21	2.94 - 3.04
D-O		1.23	1.93 - 2.01

each TiO₆ unit having two longer apical (type II, 1.99 Å) and four shorter equatorial (type I, 1.96 Å) Ti-O bonds. In H-doped rutile (TiO₂:H_i), a large distortion of the TiO₂ crystal structure near the interstitial impurity takes place, with type I bond lengths ranging from 1.90 up to 2.07 Å, and similar but less pronounced distortions of type II bonds. The H atom is bound to an oxygen with a bond length of 1.23 Å and is at distance 2.21 Å from the closest Ti atom (Fig. 1). Significant distortions of the Ti-O bond lengths are found also for TiO₂:Nb_{Ti}, notably an elongation of the type I Ti-O bond for the first Ti atom adjacent to the defect (2.07 Å) and a shortening for the subsequent bond (1.90 Å). Distortions of type II bonds are less significant in the case of substitutional Nb. As for Nb-O bonds, those of type I are slightly shorter (1.94 Å) than type I Ti-O bonds, while those of type II are slightly longer (2.02 Å) than type II Ti-O bonds. The distances between Nb and the closest Ti atoms are 2.94 and 3.04 Å, to be compared to the Ti-Ti distance of 2.97 Å in pristine rutile.

B. Band gap of pristine rutile

For pristine rutile, our calculations give a fundamental gap of 1.89 eV and 3.1 eV at PBE and G₀W₀ levels, respectively. The latter value is in excellent agreement with calculations by Malashevich et al.⁴³ (3.13 eV), who used a G₀W₀[PBE] implementation within the complex gener-

alized plasmon-pole approximation described in Ref. 44.

Similar values were obtained also by other G₀W₀ studies. In particular, Kang and Hybertsen¹⁵ obtained a band gap of 3.37 eV using a full-frequency contour-deformation (FF-CD) G₀W₀[PBE] approach; similarly, Zhang et al.⁴⁵ found 3.30 eV by full-frequency G₀W₀[LDA]; Patrick and Giustino⁴⁶ obtained 3.40 eV at the G₀W₀[PBE] level with the GN-PPM; Baldini et al.⁴⁷ obtained 3.30 eV using G₀W₀[PBE] with the PPM of Hybertsen and Louie⁴⁸; Chiodo et al.⁴⁹ reported a gap of 3.59 eV using G₀W₀[PBE] with GN-PPM.

Overall, the differences between our results and previous studies can be attributed to the different approach adopted to evaluate the frequency dependence of the self energy (Plasmon-pole Model PPM vs full-frequency methods and different flavours of PP model). In the case of Ref. [49], however, we explicitly verified that differences from our results can be due to the pseudopotential dataset used in that work. In this regard, we notice that a recent study⁵⁰ on the verification and validation of GW data across three widely used GW codes (Yambo,^{38,39} Abinit,⁵¹ and BerkeleyGW⁵²) found excellent agreement among the results obtained with these codes when the same pseudopotential dataset was used. GN-PPM and FF-CD GW methods were also compared and found to lead to a difference of the order of 0.1 eV for the fundamental gap of TiO₂ (changing from 3.2 eV with GN-PPM to 3.3 eV for FF-CD) when using (Fritz-Haber-Institute) FHI pseudopotentials with 12 valence electrons.

C. Quasi-particle levels

Figure 1 shows the unit cells of the relaxed structures of H- and Nb-doped TiO₂ together with the spin density associated with the donor states (in orange). We can see that for both H- and Nb-doped rutile the donated electron localizes on the neighbouring Ti atoms, even though with different distributions. The structural distortion close to the defect coupled to this density localization indicates the formation of localized polaronic states. Our results for H-doped rutile agree with recent FTIR experiments¹¹, which have provided evidence of small electron polarons, each bound to a Ti atom adjacent to the OH group of the hydrogen defect.

To evaluate the energy levels of the defect states in the TiO₂ band gap, we first examine the Density of States (DOS), and align the different DOS at the valence band maximum (VBM), which is little affected by the dopants (Fig. 2). At the KS-PBE level (left panels), defect states are found at the bottom of the TiO₂ conduction band. In the right panels, we show the same DOS after inclusion of quasi-particle corrections at the G₀W₀[PBE] level. In this case we clearly see defect states below the conduction bands, at 2.15 and 2.18 eV above the VBM for H and Nb, respectively. These energies correspond to -0.95 and -0.92 eV when referenced to the conduction band minimum (CBm) of pristine rutile. Similar values

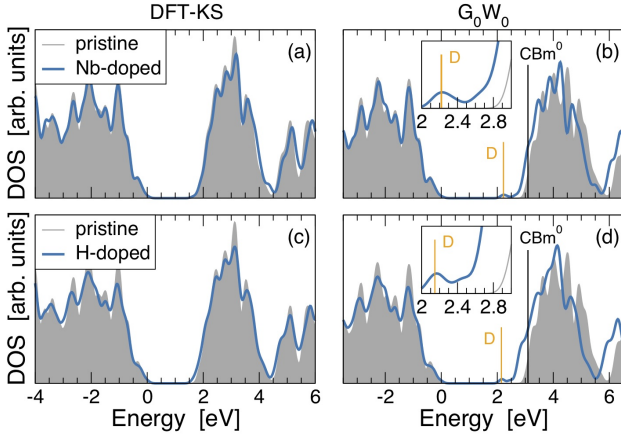


FIG. 2: K

S-DFT (PBE) and G_0W_0 DOS for the pristine (grey area), H-doped, and Nb-doped (blue curves) rutile TiO_2 . A Gaussian broadening of 0.01 Ry is used. In each panel, the energy is referred to the valence band maximum. Vertical lines indicate the position of the defect states (marked as D) and the CBm of pristine TiO_2 (marked as CBm^0). Spin resolved G_0W_0 DOS are reported in the Supplementary Material Fig. S7.

have been reported in previous theoretical studies. For H-doped rutile, defect levels at 1.0⁵⁴ and 0.97 eV⁵⁵ below the CBm have been obtained using DFT+U, while hybrid HSE06 calculations predicted vertical defect ionization energies of 0.82 and 0.86 eV for H- and Nb-doped rutile, respectively.⁵⁶

The positions of the defect levels relative to the CBm of the doped system are more difficult to assess, because the CBm itself is not clearly defined due to dopant- TiO_2 hybridization effects and an overall downshift of the conduction band. Besides the appearance of the defect states below the conduction bands (indicated with D), Figs. 2(b,d) indeed show also an overall down-shift of the conduction band of $\text{TiO}_2\text{:H}_i$ and $\text{TiO}_2\text{:Nb}_{\text{Ti}}$ with respect to its position in pristine rutile (shaded area). This effect, already observed in Ref. 57, is captured only after GW corrections and can be ascribed to enhanced screening effects due to the presence of the defects.

In Fig. 3 we show the unfolded quasi-particle band structures for the doped systems, from Eq. (4), compared to pristine rutile. We can recognize the presence of defect states below the CBm, as indicated by the non-dispersive bands along selected symmetry lines that can be attributed to localized states. Above these bands but still below the CBm of pristine TiO_2 , additional blurry features are present. The color scale represents the value of the κ -resolved DOS, as defined in Eq. (4): In each panel, black corresponds to zero and yellow to the maximum value of the DOS. The sharper the DOS (i.e. the brighter the corresponding peak), the less hybridized the defect states. Within a mean field description, at fixed κ -vector a delta peak would indeed show at the energy of each band if no defects were present. In the pres-

ence of defects instead, each peak is broadened because of the broken translational symmetry and the hybridization: the more blurred the picture, the larger the hybridization induced by the defect. The features above the non dispersive bands and below the CBm of pristine rutile can be thus attributed to such strongly hybridized states. Comparing H- and Nb-doped TiO_2 , a slightly higher degree of hybridization is apparent in $\text{TiO}_2\text{:H}_i$, which is consistent with the interstitial vs substitutional configuration of the defect.

The quasi-particle band structures for the minority spin-down states of pristine and doped TiO_2 (Fig. S6) and the spin resolved G_0W_0 density of states (Fig. S7) are shown in the Supplementary Material. From Fig. S6, it appears that the non-dispersive bands of defect states are now missing (as expected), and an overall ~ 0.2 eV down-shift of the conduction bands of the doped systems relative to pristine rutile is present, due to the enhanced screening induced by the doping. We also notice that the conduction band minima for the down-spin states of the doped systems are well-defined, suggesting they may represent the "true CBms" for the doped systems. This assumption, supported also by Fig. S7, results in defect levels lying at -0.76 and -0.87 eV for $\text{TiO}_2\text{:H}_i$ and $\text{TiO}_2\text{:Nb}_{\text{Ti}}$, respectively.

These results appear to disagree with the recent GW study by Chen et al.⁵⁷ which concluded that the deep defect level at about 0.8-1 eV below the CBm of rutile can only originate from Ti interstitials, whereas oxygen vacancies and polarons can only give rise to shallow states. As pointed out also by Chen et al, the origin of the gap state has been debated extensively in the experimental literature, where the current view is that both interstitials and oxygen vacancies contribute to the deep gap states.^{58,59} From a purely theoretical perspective, on the other hand, a firm conclusion may require not only well converged GW studies using different starting band-structures but also the study of different defect concentrations.

D. Optical properties

Pristine rutile. Our computed BSE and independent particle (GW-RPA) spectra of pristine rutile are presented in Fig 4(a). The onset of the absorption in the BSE spectrum is at ~ 3.0 eV, followed by an intense narrow peak at 3.7 eV and a shoulder at ~ 4.4 eV. Fig. 5(a) further shows that the spectrum is anisotropic, with a characteristic double peaked structure for light polarized in the [001] direction, as already reported in previous calculations.^{47,60} Both the onset and the shape of the calculated spectrum are in agreement with recent measurements,⁴⁷ which show an onset at ~ 3 eV, followed by a sharp peak at 3.93 eV, a shoulder at 4.51 eV and a broader peak at 5.42 eV. (We note that a larger number of bands in BSE and more k-points than used in the present calculations would be needed in order to reproduce also

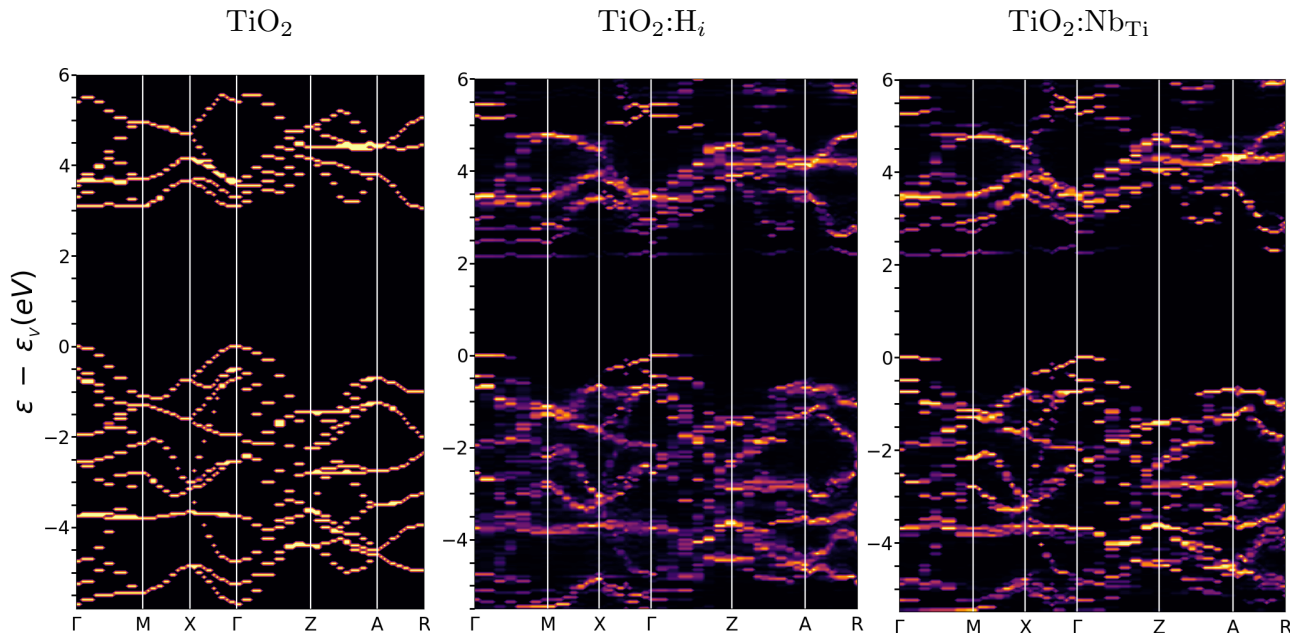


FIG. 3: Unfolded quasi-particle band-structure for pristine, $\text{TiO}_2\text{:H}_i$ and $\text{TiO}_2\text{:Nb}_{\text{Ti}}$. Results for spin-up channels are shown; results for spin down channels (which do not show any defect-related state) are reported in the Supplementary Material (Fig. S6). The color scale is such that black – yellow correspond to $[0,1]$ (in arbitrary units).

the high energy features of the experimental spectrum). Our results are also in line with recent^{47,49,60} GW-BSE calculations: our calculated red-shift of the first bright peak (0.53 eV) with respect to the independent quasi-particle picture is comparable to the results of Chiodo *et al.*⁴⁹ and to the redshift in the computed spectra of Baldini *et al.*⁴⁷ Differences observed for the excitation energies are due mainly to the different value of the computed fundamental gap (see discussion above).

Doped rutile. Upon doping, new features in the absorption spectra appear, as shown in panels (b) and (c) of Figs. 4 and 5. The most evident hallmark of the doped systems is the appearance of absorption peaks at low energy below 2 eV.

The low energy part of the spectrum of $\text{TiO}_2\text{:H}_i$ is characterized by a broad peak that has a maximum at 0.6 eV and extends up to 2 eV. This peak involves transitions from electrons in the gap states to the conduction bands. At higher energies, in the region of the spectrum where pristine rutile absorbs, we observe a small red-shift of the onset and the maximum of the absorption band with respect to the pristine crystal (from 3.68 to 3.62 eV for the maximum). We also note that the shift of the BSE with respect to the independent particle spectrum is smaller in $\text{TiO}_2\text{:H}_i$ in comparison to that found for pristine rutile, indicating an increased screening due to the excess electrons of the dopants. A red-shift of about 0.2 eV with respect to the independent particle spectrum is also observed in the lowest-energy, defect induced part of the spectrum, indicating the formation of slightly bound excitons.

In the case of Nb-doped rutile, Fig. 4(c), the spectrum in the low energy region shows a defect induced absorption characterized by a double peaked structure with maxima at 0.35 and 0.92 eV, sharper than those found for $\text{TiO}_2\text{:H}_i$. These excitations involve transitions from the defect state to conduction bands at different energies (see Figs. S3 and S4 of the Supp. Info.), and as in the case of $\text{TiO}_2\text{:H}_i$ the BSE spectrum exhibits a redshift with respect to the independent particle one, indicating the formation of bound excitons having a binding energy of 0.2 and 0.16 eV for the first and second peak respectively. As in the case of hydrogen doping, in the higher energy region we observe again a small red-shift of the onset and the maximum of the absorption (3.64 eV) with respect to pristine rutile. More importantly, also for $\text{TiO}_2\text{:Nb}_{\text{Ti}}$ the shift of the BSE spectrum with respect to the independent particle calculation (0.3 eV) is reduced in comparison to the pristine case. Apart from the small rigid shift and an overall broadening, the shape of the absorption spectrum of rutile in the high energy region is not significantly affected by the dopants.

Figure 5 shows the absorption spectra of pristine and doped rutile for light polarized along and orthogonal to the c directions. Pristine rutile exhibits a significant optical anisotropy, associated with its tetragonal symmetry, which has been extensively studied both theoretically and experimentally.⁴⁷ The anisotropy is present also for the doped systems, as expected, and is more pronounced in the low energy part of the spectra. In particular, the two low energy peaks in $\text{TiO}_2\text{:Nb}_{\text{Ti}}$ correspond to excitations that are optically active for light polarized along orthog-

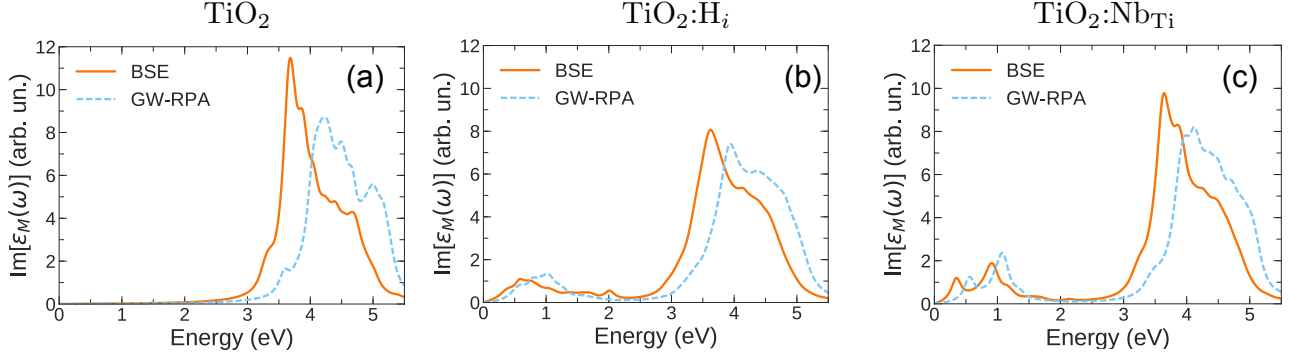


FIG. 4: The imaginary part of the dielectric constant (averaged over x,y,z polarizations) for pristine, H-doped, and Nb-doped rutile, obtained by solving the BSE and the independent quasi-particle spectra (GW-RPA).

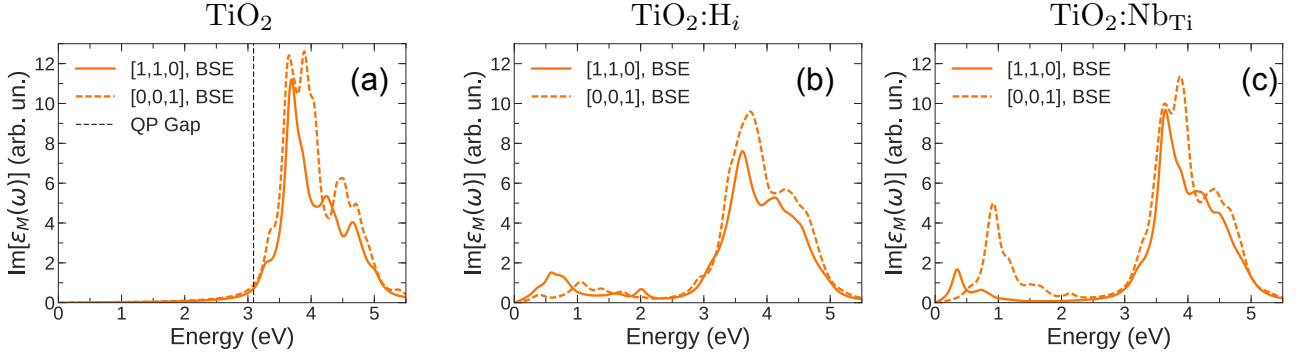


FIG. 5: Optical anisotropy in pristine, H-doped, and Nb-doped rutile, obtained using BSE. E-field polarization with respect to the direct lattice vectors is indicated in the legend.

onal directions. In order to verify that this anisotropy is not an artifact related to the small size of our supercell, we performed additional DFT-KS calculations using a $(3 \times 3 \times 4)$ supercell with 216 atoms. The results confirmed the presence of a strong anisotropy in the low energy part of the independent particle spectrum (see Fig. S8 in the SI).

Figure 6 shows the real space excitonic wave functions corresponding to the lowest energy excitations of $\text{TiO}_2:\text{H}_i$ (top panel) and $\text{TiO}_2:\text{Nb}_{\text{Ti}}$ (bottom panel), which have very similar energies, 0.33 eV in $\text{TiO}_2:\text{H}_i$ and 0.35 eV in $\text{TiO}_2:\text{Nb}_{\text{Ti}}$. In order to obtain the exciton density, in both panels of Figure 6 the position of the hole (indicated by h) was chosen in a region of high density of the occupied states mainly contributing to the excitation (see Figs. S1 and S3 in Supp. Info). We see that these excitations have very different spatial distributions in the two systems: while in $\text{TiO}_2:\text{H}_i$ the electron is strongly localized on the Ti atom closest to the defect, it is almost completely delocalized in $\text{TiO}_2:\text{Nb}_{\text{Ti}}$. In $\text{TiO}_2:\text{H}_i$ the exciton is indeed composed of transitions from the gap state to conduction states mainly localized on the adjacent Ti atoms (see Fig. S1), whereas in $\text{TiO}_2:\text{Nb}_{\text{Ti}}$ it originates completely from the transition from the defect state to the lowest conduction band that is delocalized over Ti

rows away from the defect (see Fig. S3). These characteristics are not restricted to the lowest excitations. A similar behaviour is indeed found also for other excitons at low energies: a localized wavefunction at 0.57 eV in $\text{TiO}_2:\text{H}_i$ and a delocalized exciton at 0.94 eV in $\text{TiO}_2:\text{Nb}_{\text{Ti}}$ (see Figs. S2 and S4 in SI). At higher energy, the excitonic wavefunctions corresponding to the bright peak at 3.62 and 3.64 eV in $\text{TiO}_2:\text{H}_i$ and $\text{TiO}_2:\text{Nb}_{\text{Ti}}$ (Fig.S5) are delocalized, with a shape very similar to that of the exciton at 3.68 eV in pristine rutile, confirming the small impact of dopants on the absorption spectra in the high energy region.

IV. CONCLUSIONS

The introduction of dopants into the rutile TiO_2 lattice leads to significant modification of the materials electronic and optical properties. Both interstitial Hydrogen and substitutional Niobium create a distortion of the crystal lattice around the defect and introduce electronic states localized mainly on adjacent Ti atoms. The resulting quasi-particle defect states form non dispersive bands with energies in the band gap at ~ 2.2 eV above the VBM, which corresponds to ~ -0.9 eV relative to the

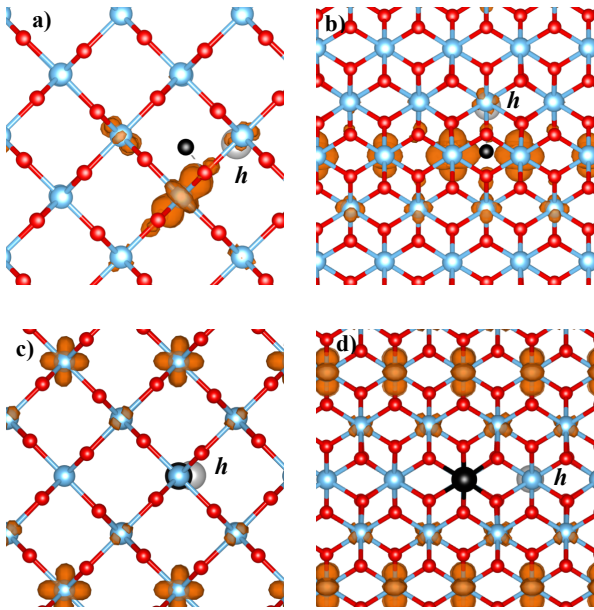


FIG. 6: Excitonic wavefunctions corresponding to the absorption peaks at 0.33 eV in $\text{TiO}_2\text{:H}_i$ (a,b) and 0.35 eV in $\text{TiO}_2\text{:Nb}_{\text{Ti}}$ (c,d). The view is along [001] in (a,c), and along [010] in (b,d). H and Niobium are shown in black; The position of the hole is indicated by a grey sphere and marked with h .

CBm of pristine rutile. The positions of the defect states relative to the CBm of doped rutile are more difficult to estimate due to the hybridization between dopant and Ti states, combined with an overall down-shift of the conduction band. A reasonable choice is however to take the CBm for the minority spin channel, which is well-defined in our calculations, as the “true CBm” for the doped sys-

tem. With this reference, our results predict the defect states to be at ~ -0.8 eV below the CBm, consistent with experimental observations.

While the high energy part of the optical spectrum (> 3 eV) is little affected by the presence of the dopant states, transition from the gap states to the conduction band give rise to new absorption peaks at low energy (< 2 eV) that enhance the absorption of rutile in the solar spectrum range. Interestingly, we found very different excitonic wavefunctions for the low energy excitations in H- and Nb doped rutile: while photoexcited electrons are largely delocalized in $\text{TiO}_2\text{:Nb}_{\text{Ti}}$, they remain localized close to the hole in $\text{TiO}_2\text{:H}_i$. These characteristics suggest a longer exciton lifetime and a larger mobility of photoexcited electrons in $\text{TiO}_2\text{:Nb}_{\text{Ti}}$, consistent with the use of Nb as an efficient dopant for improving the performance of TiO_2 in technological applications.

V. ACKNOWLEDGMENTS

We thank Ivan Marri for helpful discussions about pseudopotential accuracy in describing TiO_2 . We acknowledge support from the European Union H2020-INFRAEDI-2018-1 programme under grant agreement No. 824143 project “MaX - materials design at the exascale”. We acknowledge the use of the AiiDA⁶¹ platform, a tool for automated high throughput computational science. Computational resources were partly provided by PRACE (Grant No. Pra12_3100) on the Fermi and Marconi machines at CINECA. M.J.C. acknowledges support from Brazilian Ministry of Science and Technology grant INEO, and Brazilian National Council for Scientific and Technological Development (CNPq) Brazil, and CNR-Istituto Nanoscienze, Modena, Italy.

-
- * Electronic address: danielle.varsano@nano.cnr.it
- ¹ M. Grätzel, *nature* **414**, 338 (2001).
 - ² U. Diebold, *Surface science reports* **48**, 53 (2003).
 - ³ R. Asahi, T. Morikawa, T. Ohwaki, K. Aoki, and Y. Taga, *Science* **293**, 269 (2001).
 - ⁴ C. Di Valentin, G. Pacchioni, A. Selloni, S. Livraghi, and E. Giamello, *J. Phys. Chem. B* **109**, 11414 (2005).
 - ⁵ C. Di Valentin, G. Pacchioni, and A. Selloni, *J. Phys. Chem. C* **113**, 20543 (2009).
 - ⁶ C. Di Valentin and G. Pacchioni, *Catalysis today* **206**, 12 (2013).
 - ⁷ G. Sahasrabudhe, J. Krizan, S. L. Bergman, R. J. Cava, and J. Schwartz, *Chem. Mater.* **28**, 3630 (2016).
 - ⁸ D. Morris, Y. Dou, J. Rebane, C. Mitchell, R. Egdell, D. Law, A. Vittadini, and M. Casarin, *Physical Review B* **61**, 13445 (2000).
 - ⁹ M. Stavola, F. Bekisli, W. Yin, K. Smithe, W. Beall Fowler, and L. A. Boatner, *Journal of Applied Physics* **115**, 012001 (2014).
 - ¹⁰ H. Sezen, M. Buchholz, A. Nefedov, C. Natzeck, S. Heissler, C. Di Valentin, and C. Wöll, *Scientific reports* **4**, 3808 (2014).
 - ¹¹ A. Hupfer, L. Vines, E. Monakhov, B. Svensson, and F. Herklotz, *Physical Review B* **96**, 085203 (2017).
 - ¹² M. Gerosa, C. Bottani, C. Di Valentin, G. Onida, and G. Pacchioni, *Journal of Physics: Condensed Matter* **30**, 044003 (2017).
 - ¹³ L. Thulin and J. Guerra, *Phys. Rev. B* **77**, 195112 (2008).
 - ¹⁴ L. Chiodo, J. M. García-Lastra, D. J. Mowbray, A. Rubio, and A. Iacomino, in *Computational Studies of New Materials II: From Ultrafast Processes* (World Scientific, 2011), pp. 301–329.
 - ¹⁵ W. Kang and M. S. Hybertsen, *Phys Rev B* **82**, 085203 (2010).
 - ¹⁶ M. Alves-Santos, L. M. M. Jorge, M. J. Caldas, and D. Varsano, *J. Phys. Chem. C* **118**, 13539 (2014).
 - ¹⁷ W. Kohn and L. J. Sham, *Phys. Rev.* **140**, A1133 (1965).
 - ¹⁸ P. Giannozzi, S. Baroni, N. Bonini, M. Calandra, R. Car, C. Cavazzoni, Davide Ceresoli, G. L. Chiarotti, M. Cococcioni, I. Dabo, et al., *J. Phys. Condens. Matter* **21**, 395502 (2009).

- (2009).
- ¹⁹ P. Giannozzi, O. Andreussi, T. Brumme, O. Bunau, M. B. Nardelli, M. Calandra, R. Car, C. Cavazzoni, D. Ceresoli, M. Cococcioni, et al., *J. Phys. Condens. Matter* **29**, 465901 (2017).
 - ²⁰ J. P. Perdew, K. Burke, and M. Ernzerhof, *Phys. Rev. Lett.* **77**, 3865 (1996).
 - ²¹ D. R. Hamann, *Phys Rev B* **88**, 085117 (2013).
 - ²² M. Cococcioni and S. de Gironcoli, *Phys. Rev. B* **71**, 035105 (2005).
 - ²³ E. Finazzi, C. Di Valentin, G. Pacchioni, and A. Selloni, *J. Chem. Phys.* **129**, 154113 (2008).
 - ²⁴ B. J. Morgan and G. W. Watson, *Surf. Sci.* **601**, 5034 (2007).
 - ²⁵ G. Mattioli, F. Filippone, P. Alippi, and A. Amore Bonapasta, *Phys Rev B* **78**, 241201 (2008).
 - ²⁶ M. Setvin, C. Franchini, X. Hao, M. Schmid, A. Janotti, M. Kaltak, C. G. Van de Walle, G. Kresse, and U. Diebold, *Physical review letters* **113**, 086402 (2014).
 - ²⁷ Y. Zhao, T. Hou, Y. Li, K. S. Chan, and S.-T. Lee, *Appl. Phys. Lett.* **102**, 171902 (2013).
 - ²⁸ C. Dette, M. A. Pérez-Osorio, C. S. Kley, P. Punke, C. E. Patrick, P. Jacobson, F. Giustino, S. J. Jung, and K. Kern, *Nano Lett.* **14**, 6533 (2014).
 - ²⁹ S. Selcuk, X. Zhao, and A. Selloni, *Nature Materials* (2018).
 - ³⁰ U. Aschauer and A. Selloni, *Physical Chemistry Chemical Physics* **14**, 16595 (2012).
 - ³¹ D. T. Cromer and K. Herrington, *J. Am. Chem. Soc.* **77**, 4708 (1955).
 - ³² G. Onida, L. Reining, and A. Rubio, *Rev. Mod. Phys.* **74**, 601 (2002).
 - ³³ W. Hanke and L. J. Sham, *Phys Rev Lett* **33**, 582 (1974).
 - ³⁴ W. Hanke and L. J. Sham, *Phys Rev B* **21**, 4656 (1980).
 - ³⁵ G. Strinati, H. J. Mattausch, and W. Hanke, *Phys Rev B(R)* **25**, 2867 (1982).
 - ³⁶ G. Strinati, *Rivista Nuovo Cimento* **11**, 1 (1988).
 - ³⁷ R. W. Godby and R. J. Needs, *Phys. Rev. Lett.* **62**, 1169 (1989).
 - ³⁸ A. Marini, C. Hogan, M. Grüning, and D. Varsano, *Comput. Phys. Commun.* **180**, 1392 (2009).
 - ³⁹ D. Sangalli, C. Hogan, A. Ferretti, D. Varsano, M. Grüning, M. Palummo, C. Attaccalite, E. Cannuccia, M. Marsili, F. Affinito, et al., preprint (2018).
 - ⁴⁰ V. Popescu and A. Zunger, *Phys. Rev. B* **85**, 085201 (2012).
 - ⁴¹ P. V. C. Medeiros, S. S. Tsirkin, S. Stafström, and J. Björk, *Phys Rev B* **91**, 041116 (2015).
 - ⁴² P. V. C. Medeiros, S. Stafström, and J. Björk, *Phys Rev B* **89**, 041407 (2014).
 - ⁴³ A. Malashevich, M. Jain, and S. G. Louie, *Phys Rev B* **89**, 075205 (2014).
 - ⁴⁴ S. B. Zhang, D. Tománek, M. L. Cohen, S. G. Louie, and M. S. Hybertsen, *Phys. Rev. B* **40**, 3162 (1989).
 - ⁴⁵ M. Zhang, S. Ono, N. Nagatsuka, and K. Ohno, *Phys. Rev. B* **93**, 155116 (2016).
 - ⁴⁶ C. E. Patrick and F. Giustino, *J. Phys. Condens. Matter* **24**, 202201 (2012).
 - ⁴⁷ E. Baldini, A. Dominguez, L. Chiodo, E. Sheveleva, M. Yazdi-Rizi, C. Bernhard, A. Rubio, and M. Chergui, *Phys Rev B* **96**, 041204 (2017).
 - ⁴⁸ M. S. Hybertsen and S. G. Louie, *Phys. Rev. B* **34**, 5390 (1986).
 - ⁴⁹ L. Chiodo, J. M. García-Lastra, A. Iacomino, S. Ossicini, J. Zhao, H. Petek, and A. Rubio, *Phys. Rev. B* **82**, 045207 (2010).
 - ⁵⁰ T. Rangel, M. Del Ben, D. Varsano, G. Antonius, F. Bruneval, F. da Jornada, M. van Setten, O. Orhan, D. D. O'Regan, A. Canning, et al., preprint (2018).
 - ⁵¹ X. Gonze, B. Amadon, P.-M. Anglade, J.-M. Beuken, F. Bottin, P. Boulanger, F. Bruneval, D. Caliste, R. Caracas, M. Côté, et al., *Comput. Phys. Commun.* **180**, 2582 (2009).
 - ⁵² J. Deslippe, G. Samsonidze, D. A. Strubbe, M. Jain, M. L. Cohen, and S. G. Louie, *Comput. Phys. Commun.* **183**, 1269 (2012).
 - ⁵³ A. Hupfer, L. Vines, E. V. Monakhov, B. G. Svensson, and F. Herklotz, *Phys Rev B* **96**, 085203 (2017).
 - ⁵⁴ F. Filippone, G. Mattioli, P. Alippi, and A. Amore Bonapasta, *Phys. Rev. B* **80**, 245203 (2009).
 - ⁵⁵ J. Stausholm-Møller, H. H. Kristoffersen, B. Hinnemann, G. K. H. Madsen, and B. Hammer, *J. Chem. Phys.* **133**, 144708 (2010).
 - ⁵⁶ P. Deák, B. Aradi, and T. Frauenheim, *Phys. Rev. B* **83**, 155207 (2011).
 - ⁵⁷ T. Chen, Y.-n. Hao, F. Jin, M. Wei, J. Feng, R. Jia, Z. Yi, M. Rohlfing, C. Liu, and Y. Ma, *Physical Review B* **98**, 205135 (2018).
 - ⁵⁸ C. L. Pang, R. Lindsay, and G. Thornton, *Chemical reviews* **113**, 3887 (2013).
 - ⁵⁹ W.-J. Yin, B. Wen, C. Zhou, A. Selloni, and L.-M. Liu, *Surface Science Reports* **73**, 58 (2018).
 - ⁶⁰ M. Landmann, E. Rauls, and W. G. Schmidt, *J. Phys. Condens. Matter* **24**, 195503 (2012).
 - ⁶¹ G. Pizzi, A. Cepellotti, R. Sabatini, N. Marzari, and B. Kozinsky, *Comput. Mater. Sci.* **111**, 218 (2016).